

2 Initial results of NEXT-DEMO, a large-scale 3 prototype of the NEXT-100 experiment

The NEXT Collaboration

V. Álvarez,^a F.I.G. Borges,^b S. Cárcel,^a J. Castel,^c S. Cebrián,^c A. Cervera,^a
C.A.N. Conde,^b T. Dafni,^c T.H.V.T. Dias,^b J. Díaz,^a M. Egorov,^d R. Esteve,^e
P. Evtoukhovitch,^f L.M.P. Fernandes,^b P. Ferrario,^a A.L. Ferreira,^g E.D.C. Freitas,^b
V.M. Gehman,^d A. Gil,^a A. Goldschmidt,^d H. Gómez,^c J.J. Gómez-Cadenas,^{a*}
D. González-Díaz,^c R.M. Gutiérrez,^h J. Hauptman,ⁱ J.A. Hernando Morata,^j
D.C. Herrera,^c F.J. Iguaz,^c I.G. Irastorza,^c M.A. Jinete,^h L. Labarga,^k A. Laing,^a
I. Liubarsky,^a J.A.M. Lopes,^b D. Lorca,^a M. Losada,^h G. Luzón,^c A. Marí,^e
J. Martín-Albo,^{a†} A. Martínez,^a T. Miller,^d A. Moiseenko,^f F. Monrabal,^{a‡}
C.M.B. Monteiro,^b F.J. Mora,^e L.M. Moutinho,^g J. Muñoz Vidal,^a H. Natal da Luz,^b
G. Navarro,^h M. Nebot,^a D. Nygren,^d C.A.B. Oliveira,^{dg} R. Palma,^l J. Pérez,^k
J.L. Pérez Aparicio,^l J. Renner,^d L. Ripoll,^m A. Rodríguez,^c J. Rodríguez,^a
F.P. Santos,^b J.M.F. dos Santos,^b L. Seguí,^c L. Serra,^a D. Shuman,^d A. Simón,^a
C. Sofka,ⁿ M. Sorel,^a J.F. Toledo,^d A. Tomás,^c J. Torrent,^m Z. Tsamalaidze,^f
D. Vázquez,^j J.F.C.A. Veloso,^g J.A. Villar,^c R. Webb,ⁿ J.T. White,ⁿ N. Yahlali^a

- ^a *Instituto de Física Corpuscular (IFIC), CSIC & Universitat de València
Calle Catedrático José Beltrán, 2, 46980 Paterna, Valencia, Spain*
- ^b *Departamento de Física, Universidade de Coimbra
Rua Larga, 3004-516 Coimbra, Portugal*
- ^c *Lab. de Física Nuclear y Astropartículas, Universidad de Zaragoza
Calle Pedro Cerbuna, 12, 50009 Zaragoza, Spain*
- ^d *Lawrence Berkeley National Laboratory (LBNL)
1 Cyclotron Road, Berkeley, California 94720, USA*
- ^e *Instituto de Instrumentación para Imagen Molecular (I3M), Universitat Politècnica de València
Camino de Vera, s/n, Edificio 8B, 46022 Valencia, Spain*
- ^f *Joint Institute for Nuclear Research (JINR)
Joliot-Curie 6, 141980 Dubna, Russia*
- ^g *Institute of Nanostructures, Nanomodelling and Nanofabrication (i3N), Universidade de Aveiro
Campus de Santiago, 3810-193 Aveiro, Portugal*
- ^h *Centro de Investigaciones, Universidad Antonio Nariño
Carretera 3 este No. 47A-15, Bogotá, Colombia*
- ⁱ *Department of Physics and Astronomy, Iowa State University
12 Physics Hall, Ames, Iowa 50011-3160, USA*
- ^j *Instituto Gallego de Física de Altas Energías (IGFAE), Univ. de Santiago de Compostela
Campus sur, Rúa Xosé María Suárez Núñez, s/n, 15782 Santiago de Compostela, Spain*
- ^k *Departamento de Física Teórica, Universidad Autónoma de Madrid
Ciudad Universitaria de Cantoblanco, 28049 Madrid, Spain*
- ^l *Dpto. de Mecánica de Medios Continuos y Teoría de Estructuras, Univ. Politècnica de València
Camino de Vera, s/n, 46071 Valencia, Spain*
- ^m *Escola Politècnica Superior, Universitat de Girona
Av. Montilivi, s/n, 17071 Girona, Spain*
- ⁿ *Department of Physics and Astronomy, Texas A&M University
College Station, Texas 77843-4242, USA*

E-mail: gomez@mail.cern.ch, justo.martin-albo@ific.uv.es,

francesc.monrabal@ific.uv.es

ABSTRACT: NEXT-DEMO is a large scale prototype and demonstrator of the NEXT-100 High Pressure Xenon Gas TPC, which will search for the neutrinoless double beta decay of ^{136}Xe using 100–150 kg of enriched xenon gas. The apparatus was built to prove the expected performance of NEXT-100, namely, energy resolution better than 1% FWHM at 2.5 MeV and event topological reconstruction. In this paper we describe the operation and initial results of the detector. A resolution of 1.7% FWHM at 511 keV (0.77% FWHM at 2.5 MeV) is obtained in the full fiducial volume of the detector. A topological analysis shows that electrons are identified by the characteristic blob energy deposit associated to the Bragg peak in 98.5% of the cases, with a rate of misidentification (two blobs) of 0.14%.

KEYWORDS: Time projection chambers (TPC); Gaseous imaging and tracking detectors.

*Spokesperson

†Co-corresponding author

‡Co-corresponding author

8 Contents

9	1. Introduction	1
10	2. The NEXT-DEMO prototype	3
11	2.1 Gas system	4
12	2.2 Pressure vessel	5
13	2.3 Time projection chamber	6
14	2.4 Energy plane	7
15	2.5 Tracking plane	7
16	2.6 Electronics	10
17	3. Analysis of ^{22}Na gamma-ray data	11
18	3.1 Operating conditions	11
19	3.2 Calibration of the PMTs	12
20	3.3 Waveforms	13
21	3.4 Longitudinal and radial position	14
22	3.5 Definition of the fiducial volume	15
23	3.6 Primary scintillation	15
24	3.7 Secondary EL scintillation	19
25	4. Reconstruction of the energy spectrum	20
26	4.1 Fiducial containment condition	20
27	4.2 Geometrical corrections	21
28	4.3 Longitudinal corrections	22
29	4.4 Radial and azimuthal corrections	23
30	4.5 Energy resolution	23
31	5. The topological signal	25
32	6. Summary and outlook	28

34 1. Introduction

35 NEXT-100[1] is a High Pressure Gaseous Xenon (HPXe) time projection chamber (TPC), currently
 36 under construction at the Canfranc underground laboratory (LSC) in Spain. The apparatus will
 37 search for neutrinoless double beta decay ($\beta\beta 0\nu$) using 100–150 kg of xenon gas, enriched in
 38 the ^{136}Xe isotope to $> 90\%$. A HPXe detector boasts two essential features for $\beta\beta 0\nu$ searches:
 39 excellent *energy resolution* (better than 1% FWHM at the Q -value of ^{136}Xe) and event *topological*

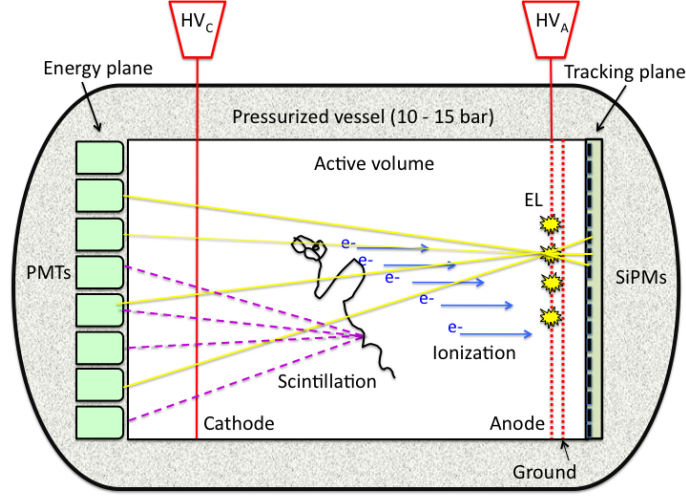


Figure 1. The *Separated, Optimized Functions* (SOFT) concept in the NEXT experiment: EL light generated at the anode is recorded in the photosensor plane right behind it and used for tracking; it is also recorded in the photosensor plane behind the transparent cathode and used for a precise energy measurement.

information for the identification of signal and background. Combining these gives NEXT an excellent experimental sensitivity to $\beta\beta 0\nu$ [2]. In addition, the technique can be extrapolated to the ton-scale, thus allowing the full exploration of the inverted hierarchy of neutrino masses.

Xenon, as a detection medium, provides both *scintillation* and *ionization* as primary signals. The former is used to establish the start-of-event time (t_0), while the latter is used for calorimetry and tracking. In its gaseous phase, xenon can provide high energy resolution, in principle as good as 0.3% FWHM at $Q_{\beta\beta} \sim 2.5$ MeV, the energy of the end-point of the spectrum for the double decay mode [3]. In order to achieve optimal energy resolution, the ionization signal is amplified in NEXT using *electroluminescence* (EL): the electrons liberated by ionizing particles passing through the gas are first drifted towards the TPC anode by a weak electric field, entering then into another region where they are accelerated by a moderate electric field, intense enough so that the electrons can excite the xenon atoms but not enough to ionize them. This excitation energy is ultimately released (with sub-poissonian fluctuations) in the form of ultraviolet photons of wavelengths near 172 nm.

NEXT-100 will have different readout systems for calorimetry and tracking, a concept called SOFT (see figure 1). An array of photomultiplier tubes (PMTs), the so-called *energy plane*, EP , located behind the TPC cathode detects a fraction of the EL light to provide a precise measurement of the total energy deposited in the gas. These PMTs detect also the primary scintillation, used to signal the start of the event (t_0). The forward-going EL light is detected by a dense array of silicon photomultipliers (SiPMs), known as the *tracking plane*, TP , located behind the anode, very close to the EL region and is used for event topological reconstruction.

During the last three years, as part of the NEXT R&D program, we have built the *NEXT-DEMO* prototype with the double aim of *demonstrating* the NEXT detector concept, and *gaining experience* that would facilitate the design, construction and operation of the NEXT-100 detector. This paper presents the initial operation and results of the prototype. The organization is as follows. Section 2 describes the initial configuration of the apparatus. Section 3 explains its characterization with

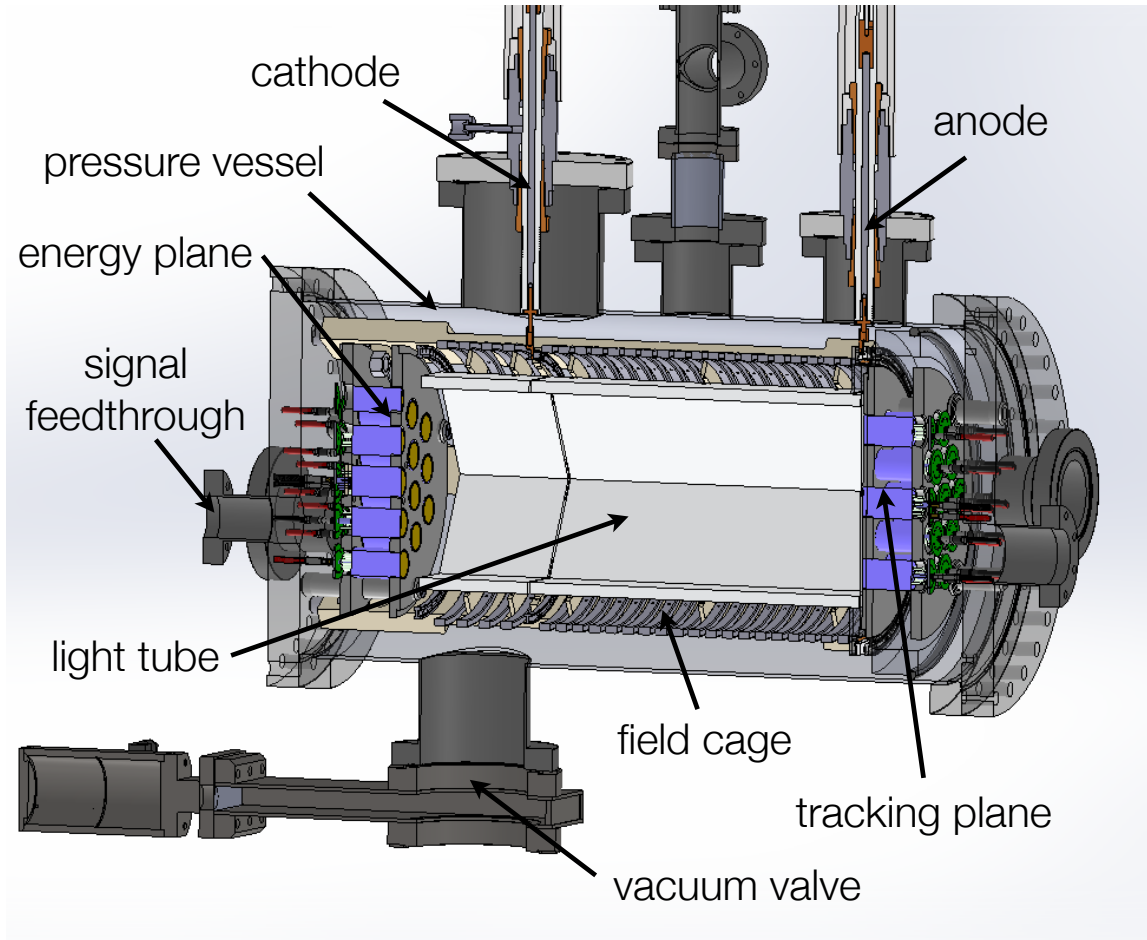


Figure 2. Cross-section drawing of the NEXT-DEMO detector.

65 ^{22}Na source. Section 4 presents our initial energy analysis, and section 5 first results on topology
 66 reconstruction. Section 6 concludes.

67 **2. The NEXT-DEMO prototype**

68 NEXT-DEMO, shown in figure 2, is a high-pressure xenon gas, electroluminescent TPC with
 69 specialized readout planes for calorimetry and tracking. Its active volume is 30 cm long and 30
 70 cm diameter. The TPC is housed in a stainless-steel pressure vessel that can withstand up to 15
 71 bar. Natural xenon circulates, in a closed loop, through the vessel and a system of purifying filters.
 72 The prototype is not radiopure and it is not shielded against natural radioactivity. Figure 2 shows a
 73 drawing of NEXT-DEMO, with all major parts labelled. The detector is installed in a semi-clean
 74 room at the *Instituto de Física Corpuscular* (IFIC), in Valencia, Spain (see figure 3).

75 The main objective of NEXT-DEMO was the validation of the detector concept to be used in
 76 NEXT-100. More specifically, the goals of the prototype were: (a) to demonstrate the topological
 77 signal in high-pressure xenon gas (HPXe); (b) to test long drift lengths and high voltages (up to 50
 78 kV in the cathode and 25 kV in the anode); (c) to understand gas recirculation in a large volume,



Figure 3. The NEXT-DEMO detector and ancillary systems in their location at a semi-clean room at IFIC.

including operation stability and robustness against leaks; (d) to understand the transmittance of the light tube.

The “permanent” elements of NEXT-DEMO are the pressure vessel (PV), field cage (FC), energy plane and high voltage feedthroughs (HVFT). The light tube (LT) has been operated with and without coating with terphenyl-butadiene (TPB), a wavelength shifter coating. We have also operated the detector with two different tracking planes, one based on PMTs and another based on MPPCs.

In this paper we describe the initial operation of NEXT-DEMO with a tracking plane implemented using 19 pressure-resistant Hamamatsu PMTs, identical to those of the energy plane, but operated at a lower gain. This is the simplest incarnation of the SOFT concept, using the same type of devices (with different gains) for tracking and energy. It relies on the availability of PMTs sensitive to the VUV light emitted by xenon and exploits the fact that PMTs can be used as energy-measuring devices and as position-sensitive detectors.

We studied the detector response under two different conditions: a) an “ultraviolet configuration”, or (UVC), in which the LT had no coating, and b) a “blue configuration”, in which the LT was coated with TPB in order to understand the improvements in light collection and resolution attained by coating the light tube with a wavelength shifter.

2.1 Gas system

The functions of the gas system of NEXT-DEMO are the vacuum evacuation of the detector, its

pressurization and depressurization with xenon (and argon), and the recirculation of the gas through purification filters. A schematic of the system is shown in figure 4.

The standard procedure during normal operation of the detector starts with the evacuation of the vessel to vacuum levels around 10^{-5} mbar, followed by an argon purge. A second vacuum step exhausts the argon from the system. The detector is then filled with xenon gas to pressures up to 15 bar. The xenon can be cryogenically reclaimed to a stainless-steel bottle connected to the gas system by simply immersing it in a dewar filled with liquid nitrogen.

The vacuum-evacuation system consists of a roughing pump (Edwards XDS5 scroll vacuum pump) and a turbo molecular pump (Pfeiffer HiPace 300). Vacuum pressures better than 10^{-7} mbar have been obtained after pumping out the detector for several days. The recirculation loop is powered by an oil-less, single-diaphragm compressor (KNF PJ24999-2400) with a nominal flow of 100 standard liters per minute. This translates to an approximate flow of 10 liters per minute at 10 bar, thus recirculating the full volume of NEXT-DEMO (~ 45 L) in about 5 minutes. The gas system is equipped with both room-temperature (SASE MC50) and heated getters (SASE PS4-MT15) that remove electronegative impurities (O_2 , H_2O , etc.) from the xenon. All the gas piping, save for the inlet gas hoses and getter fittings, are 1/2 inch diameter with VCR fittings. A set of pressure relief valves (with different settings for the various parts of the system) and a burst disk in the vacuum system protect the equipment and personnel from overpressure hazards.

The operation of the gas system has been, in general, very stable. The detector has run without interruption for long periods of up to 6 weeks with no leaks and continuous purification of the gas. However, one major leak occurred, which caused the loss of the xenon volume contained in the chamber, when the diaphragm of the recirculation pump broke. To avoid the same type of accident an emergency system that, on pressure drop, automatically closes several valves to insulate the pump from the rest of the gas system was installed. This device avoided a second catastrophic gas loss when the diaphragm of the pump broke a second time. After those two accidents the system has run without major issues, although identifying and fixing micro-leaks has been a rather involved task.

Several lessons have been learned to be applied to NEXT-100 gas system. The most important is the need of a extremely robust and reliable pump. In particular, a triple-seal all-metal pump, manufactured by SERA, has been identified as a good candidate for the gas system of NEXT-100. Concerning the getters, we have confirmed that cold getters emit radon, while the emanation of hot getters appears to be negligible. Furthermore, cold getters do not remove nitrogen. The presence of nitrogen in the xenon increases the drift velocity by between 30% and 50%, but it also seems to increase attachment.

2.2 Pressure vessel

The pressure vessel of NEXT-DEMO is a stainless steel (grade 304L) cylindrical shell, 3 mm thick, 30 cm diameter and 60 cm length, welded to Conflat (CF) flanges on both ends. Both end-caps are 3-cm thick plates with standard CF flanges. The vessel was certified to 15 bar operational pressure.

The pressure vessel was designed at IFIC and built by Trinos Vacuum Systems, a local manufacturer. Further improvements, including a rail-system to open the and move the end-caps, have been built at the mechanical workshop at IFIC.

The side of the chamber contains 8 CF40 size nipples. One set of 4 is located in the horizontal plane while the other is displaced towards the underside with respect to the first set by 30° . These

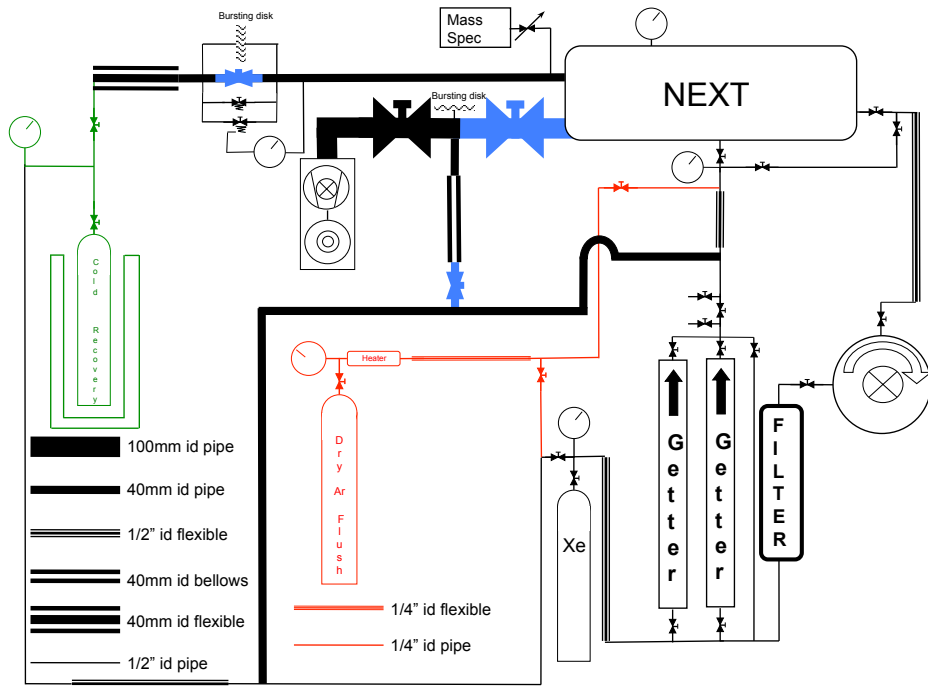


Figure 4. Simplified schematic of the gas system of NEXT-DEMO.

contain radioactive source ports used for calibration of the TPC. The ports are made by welding a 0.5 mm blank at the end of a 12 mm liquid feedthrough. In this way, calibrating radioactive sources such as ^{22}Na or a ^{137}Cs can be placed outside the detector.

2.3 Time projection chamber

The electric field in the TPC is created by supplying a large negative voltage to the transparent cathode then degrading it through metallic rings connected via resistors (field cage, FC). 30 cm from the cathode the FC ends in a transparent grid called the gate. The gate is at negative voltage so that a moderate electric field (typically of 2.5 to 3 kV/cm/bar) is created between the gate and the anode (also a transparent mesh), which is at ground. The field shaping rings of the field cage are made by cutting and machining aluminum pipe. The supports are manufactured from peek, a low outgassing plastic. Figure 6 shows a view of the field cage.

The light tube is made of teflon (PTFE) panels and has an hexagonal cross section. Figure 7 shows a view of the fiducial volume defined by the light tube.

The High Voltage is supplied to the cathode and the gate through custom made high-voltage feed throughs (HVFT). These have been tested to high vacuum and 100 kV without leaking or sparking. The HVFT designed and built by Texas A&M (as the field cage), are shown in Figure 8.



Figure 5. The pressure vessel of NEXT-DEMO.

2.4 Energy plane

The goal of the energy plane is to integrate the energy of the event as well as to measure the primary scintillation signal. This requires single-photoelectron sensitive devices such as photomultipliers (PMTs). In NEXT-DEMO, the energy plane (Figure 9) is equipped with 19 Hamamatsu R7378A PMTs. These small (1") PMTs are pressure resistant and have good quantum efficiency ($\sim 20\%$) in the VUV region. They can be used, therefore, to read directly the primary and secondary EL produced in the xenon by charged particles. The coverage of the energy plane is about 60%.

The PMTs are mounted in custom-made bases which are used as voltage dividers and also allow the extraction of the signal induced in the PMTs. This requires a total of 38 cables inside the PV connected to feed-throughs. The energy plane is located at 10 cm from the cathode in such a way that the electric field between the cathode (i.e. a maximum of some 50 kV) and the PMT plane (grounded) is less than the threshold in which EL light is produced. The threshold for EL light production is typically 0.5 kV/cm/bar. The electric field between the cathode and the PMT plane in NEXT-DEMO at 50 kV in the cathode and 10 bar is precisely that value.

Operation of the energy plane has been in general quite stable, although shorts and broken connections have appeared in some of the PMTs.

2.5 Tracking plane

One of the most important features of NEXT-100 is its ability to measure the topological signature of electrons produced in the decay of ^{136}Xe . The tracking function is provided by covering the anode

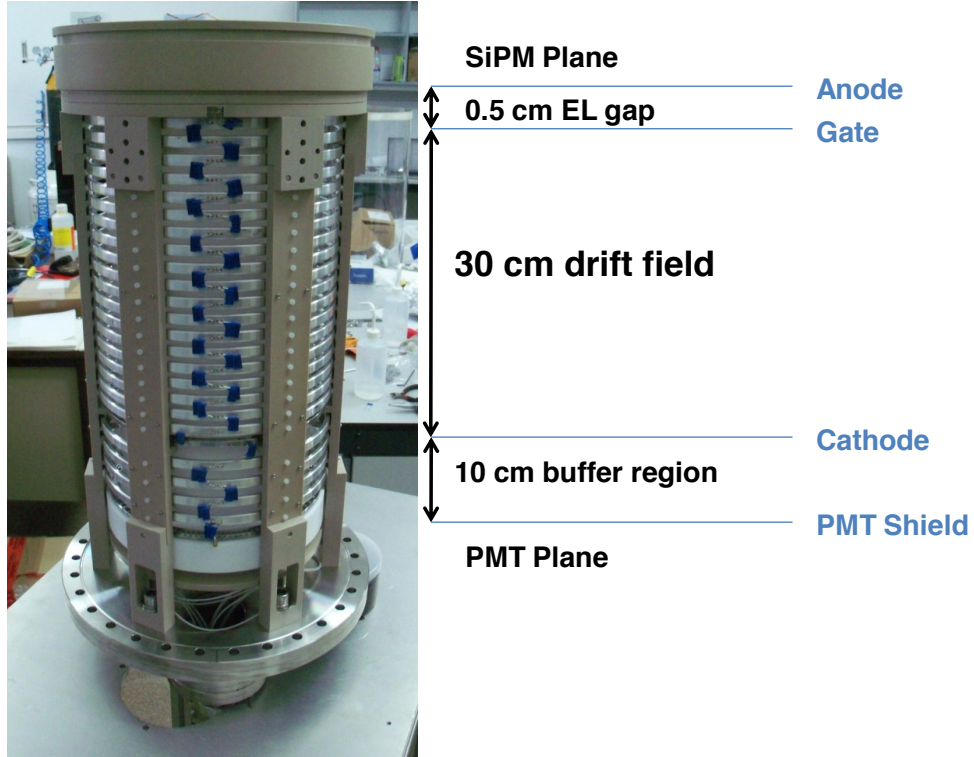


Figure 6. External view of the field cage showing the field rings, divider resistor chain. The Cathode, EL region, PMT screen and drift region are indicated.

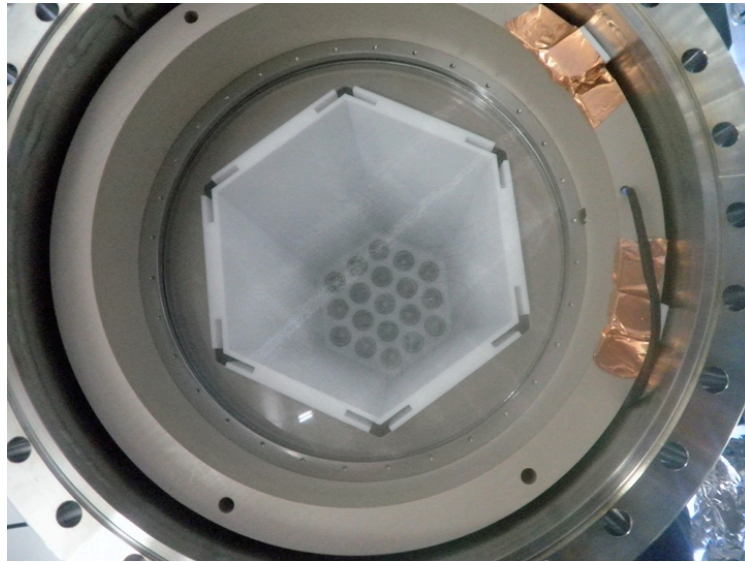


Figure 7. A view from the top of the NEXT1 field cage made of PTFE slabs. The energy plane honeycomb can be seen clearly through the transparent grids.

175 plane with detectors sensitive to light that provide the transverse coordinates (x, y) of an energy
 176 deposition while the longitudinal coordinate (z) is obtained from the drift time.

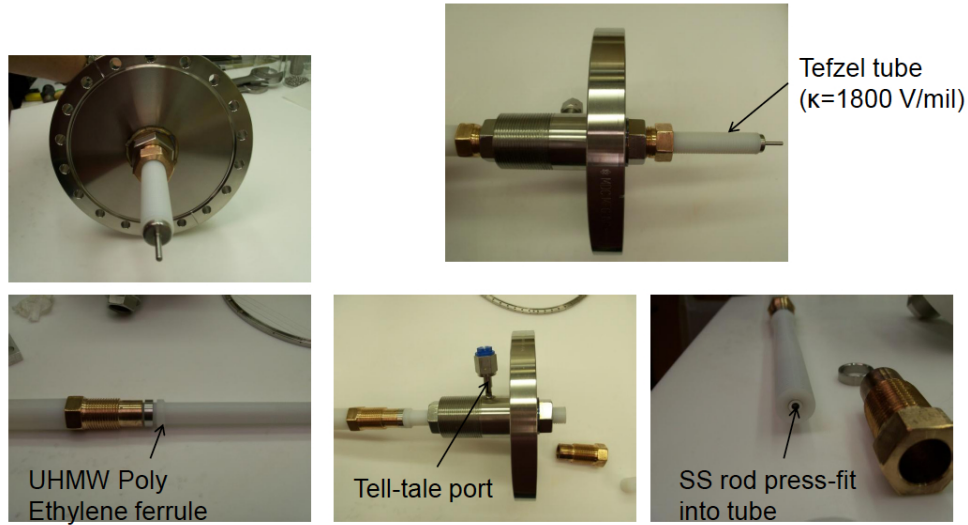


Figure 8. High-Voltage feed throughs (HVFT), designed and built by Texas A&M.

Field Cage Breakdown – PMT Plane

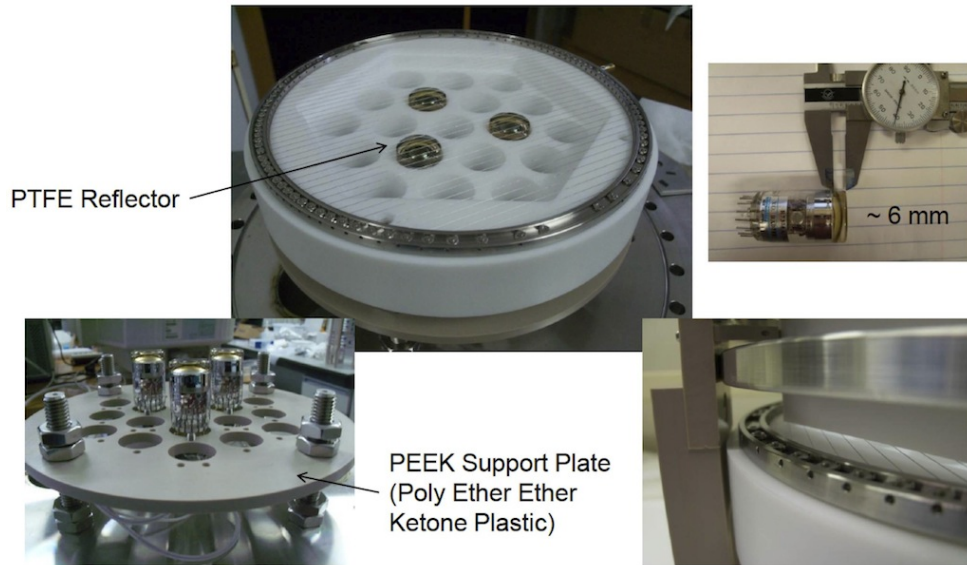


Figure 9. The NEXT-DEMO energy plane. The lower support of the energy plane PMTs is made of peek and the upper one of PTFE (which is more reflective at the relevant wavelengths). The energy plane is located behind a transparent cathode.

177 The simplest tracking plane that can be used in NEXT-DEMO involves the use of small,
 178 pressure-resistant, VUV-sensitive PMTs. Figure 10 shows the PMT tracking plane composed of 19
 179 PMTs in such a way as to mirror the Cathode plane. The PMT quartz windows are located 2 mm
 180 away from the anode grid. Position reconstruction is based on energy sharing between the PMTs,
 181 and is much better than PMT pitch.

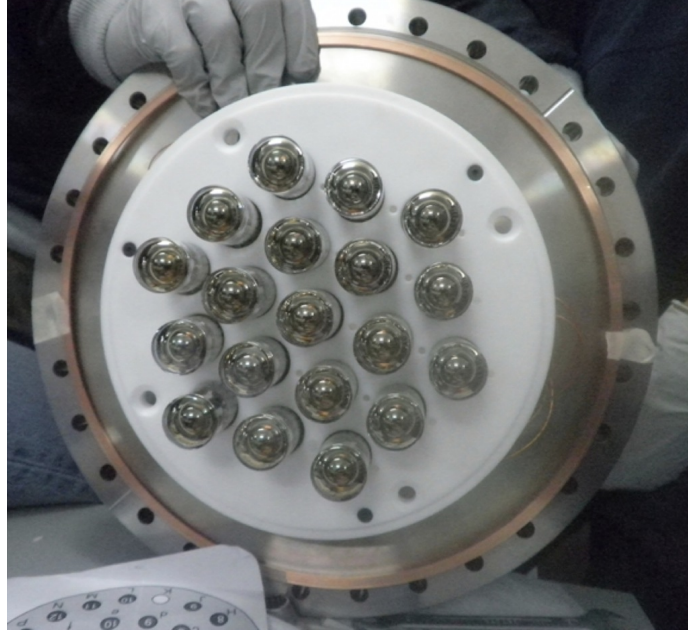


Figure 10. The PMT tracking plane installed behind the for the UV configuration of NEXT-DEMO.

2.6 Electronics

The primary signals in NEXT-DEMO can be grouped in two scales. *Primary scintillation*, which results in a fast, weak (not amplified) and rather narrow signal, and *secondary EL emissions*, which are slow, intense (amplified) and long signals. The primary scintillation results in a small but detectable number of photoelectrons per PMT. The bulk of the signal comes in about 20 ns. Since the total number of pes is small, it is not necessary to sample more quickly than this time scale.

The gain of the PMTs is adjusted to around 10^7 for the cathode—to place the mean amplitude of a single photoelectron pulse, spe, well above electronic system noise—and around 10^6 for the anode (since they record the direct EL light produced in the grids, roughly a factor 100 more light than in the cathode PMTs).

The main function of the front-end electronics of a PMT system is to shape and filter the fast signals produced by the PMTs (less than 5 ns wide) to match the digitizer and eliminate the high frequency noise which produces unwanted ringing. An integrator is implemented by simply adding a capacitor and a resistor to the PMT base. The charge integration capacitor shunting the anode stretches the pulse and reduces the primary signal peak voltage accordingly. Our design uses a single amplification stage based on a fully differential amplifier THS4511, which features low noise ($2\text{nV}/\sqrt{\text{Hz}}$) and provides enough gain to compensate for the attenuation in the following stage. Amplification is followed by a passive RC filter with a cut frequency of 800 kHz. This filtering produces enough signal stretching to allow the acquisition of many samples per single photo-electron at 40 MHz. The front-end circuit for NEXT-DEMO was implemented in 7 channel boards and connected via HDMI cables to 12-bit 40-MHz digitizer cards. These digitizers are read out by the FPGA-based DAQ modules (FEC cards) that buffer, format and send event fragments to the DAQ PCs. As for the FEC card, the 16-channel digitizer add-in card was designed in a joint effort

205 between CERN and the NEXT collaboration within the RD-51 R&D program. These two cards are
 206 edge mounted to form a standard 6U220 mm eurocard. An additional FEC module with a different
 207 plug-in card is used as trigger module. Besides forwarding a common clock and commands to all
 208 the DAQ modules, it receives trigger candidates from the DAQ modules, runs a trigger algorithm in
 209 the FPGA and distributes a trigger signal. The trigger electronics also accepts external triggers for
 210 detector calibration purposes.

211 3. Analysis of ^{22}Na gamma-ray data

212 The response of the NEXT-DEMO detector has been studied using the 511 keV gammas emitted
 213 by a weak ^{22}Na source. The photons interacting in the gas produce an electron via Compton or
 214 photoelectric interaction. The total energy deposited in the detector by these electrons is then
 215 calculated using the EL light produced as described in section 2.4.

216 Fitting the photo peak determines the effective energy resolution of the chamber which is a
 217 combination of the intrinsic resolution (due to the xenon Fano factor) and several instrumental
 218 effects. These include photoelectron statistics (e.g, the number of photoelectrons in the PMTs per
 219 primary ionization electron), electronics noise and the residual effect due to the various corrections
 220 that need to be applied to the raw spectrum (see [4] for a detailed study of resolution effects in NEXT
 221 prototypes). Furthermore, the topological signal can be studied, selecting electrons of different
 222 energies.

223 3.1 Operating conditions

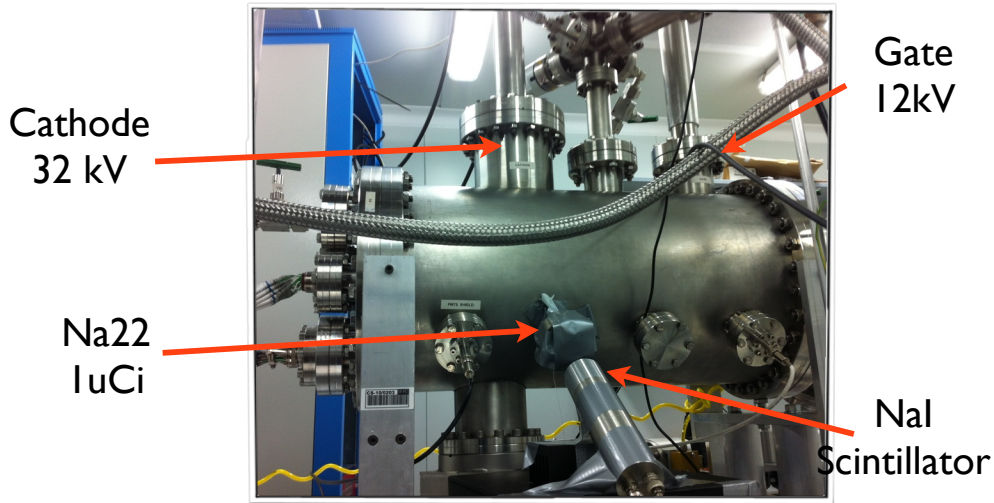


Figure 11. A view of NEXT-DEMO.

224 The detector was operated under the following conditions:

- 225 • **Pressure:** 10 bar.
- 226 • **Drift field:** Varied between 300 V/cm and 700 V/cm. The default value was -20 kV across
- 227 30 cm or 666 V/cm.

- **EL field:** Varied between 2.0 kV/cm/bar and 3 kV/cm/bar. The default value was 12 kV across 0.5 cm at 10 bar, corresponding to 2.4 kV/cm/bar.
- **Source:** A ^{22}Na source of 1 μCi activity, located in a port very near the cathode.

The typical configuration, illustrated in figure 11, required -32kV at the cathode and -12 kV at the gate. Operation has been smooth in general, although occasional sparks in the anode-gate grids due to dust or corona discharge were not uncommon. In normal operation, the spark rate decreases as the gas becomes cleaner (and the dust specs are burned by previous sparks), until reaching a rate of about 1 spark every few days, which introduces very little distortion in the data taking.

The use of a ^{22}Na source allows the tagging of the events with a small NaI calorimeter (shown in figure 11) exploiting the fact that ^{22}Na emits a positron which results, upon annihilation, in two back-to-back, 511 keV gammas. The NaI calorimeter records the backward going gamma, allowing an external trigger if desired and providing a time window to locate the scintillation signal of the gamma interacting in the chamber. This facilitates the selection of a minimally biased sample.

The trigger used to select ^{22}Na events is formed by the delayed coincidence (in a 400 μs window) of the NaI channel and one PMT from the energy plane. The PMT energy is required to be between two thresholds, T_{\min} , which separates the S_2 signal candidate from primary scintillation, and T_{\max} , which separates ^{22}Na events from other type of interactions (such as alpha particles). The PMT reading the NaI channel is required to have a signal consistent with the photoelectric interactions of the 511 keV ^{22}Na gamma.

The trigger rate with this particular set of conditions was 1.5 Hz which is consistent with the rate expected from the (weak) tagged source according to the MC. Other trigger schemes have been tested, such as varying the threshold and adding more PMTs to the coincidence but most of the data was taken with the trigger described above on the grounds of its simplicity. The trigger, however, tends to bias the spectrum, enhancing the selection of electrons of high energy in the photoelectric peak, at the expenses of the Compton spectrum.

3.2 Calibration of the PMTs

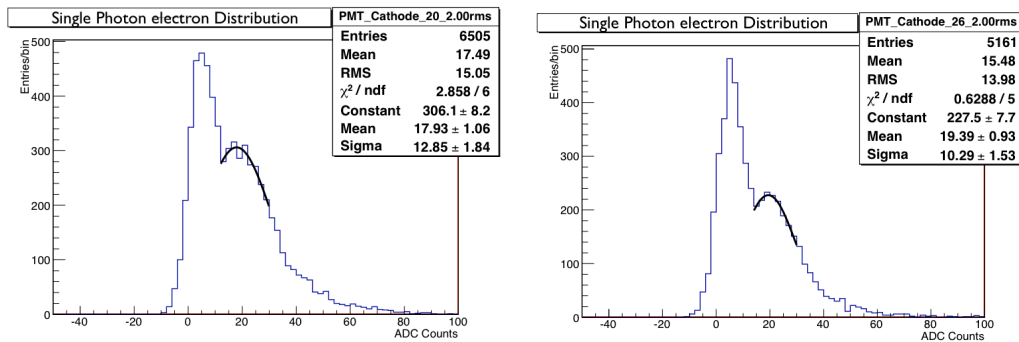


Figure 12. An example of the procedure to measure the gain of the Cathode PMTs. The plane is illuminated with a weak light emanating from a diode located in the tracking plane and pulses are recorded. The single photoelectron peak (spe) is clearly distinguishable from the background. The two PMTs shown in the example have similar gains.

254 The 19 PMTs in the energy plane are operated at a gain of around 5×10^6 . To equalize them,
 255 we have installed a LED in the tracking plane which illuminates the PMTs of the energy plane. The
 256 LED intensity is regulated so that single photoelectron pulses (spe) can be recorded in the cathode
 257 PMTs, as illustrated in figure 12.

258 Once the cathode PMTs have been equalized it is possible to sum the contribution of all the
 259 PMTs in the energy plane. Primary and secondary scintillation signals (S_1 and S_2) are studied using
 260 this sum, expressed in photoelectrons (pes).

261 The 19 PMTs of the tracking plane are operated at a lower gain (2×10^6) since they receive
 262 much more light than the energy plane PMTs and a higher gain would mean saturation was more
 263 probable. At this lower gain, it is not possible to separate the spe peak from the background peak.
 264 However, since the PMTs are not used to measure the absolute energy of the event, it is not necessary
 265 to determine their absolute gain. Rather, they are equalized by illuminating them with a diode and
 266 fitting the PMT response to a gaussian. This determines a weight:

$$w = \frac{1}{A} \quad (3.1)$$

267 where A is the amplitude recorded by the PMT (in ADC counts).

268 3.3 Waveforms

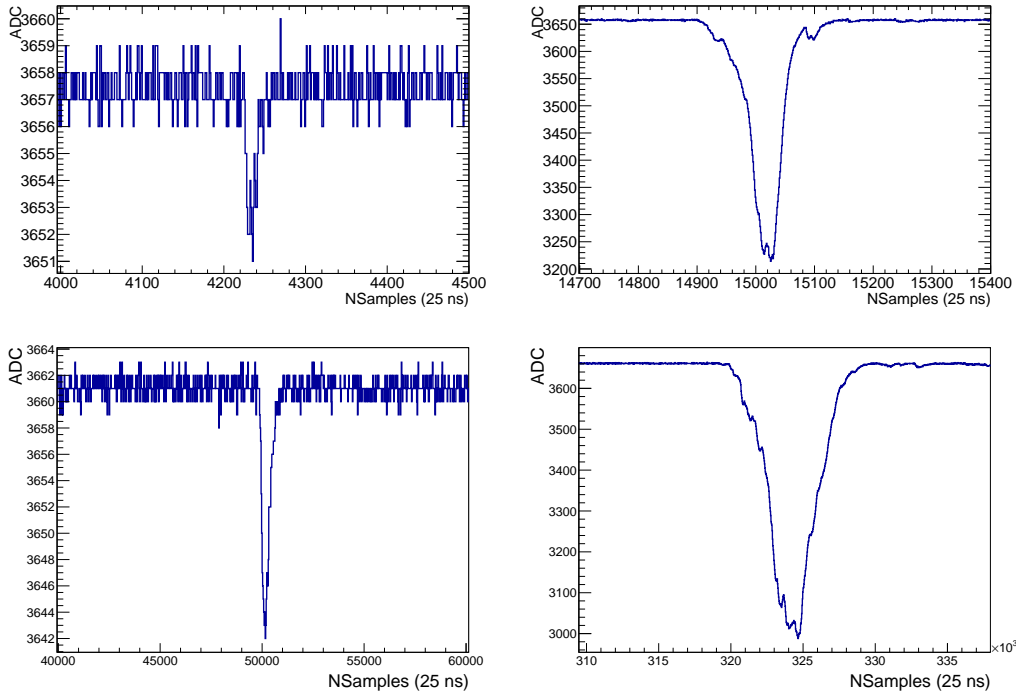


Figure 13. Raw waveforms, showing the typical shape of S_1 (left) and S_2 (right). The waveforms are measured using the equalized sum of all the cathode PMTs. The top waveform corresponds to the UVC, the bottom row to the BC.

269 Figure 13-top shows the raw waveforms corresponding to S_1 and S_2 signals in the UVC run.
 270 The waveform is computed using the equalized sum of all the cathode PMTs, which is resampled

before searching for S_1 -like and S_2 -like peaks. The former are narrow and exponential-like (the peak of the signal is typically found in the first or second bin after resampling and the signal damps very quickly). The later are Gaussian-like, and much wider. As figure 13 shows, the signal is well above the background, allowing an easy identification of the waveforms.

3.4 Longitudinal and radial position

The interaction of the 511 keV ^{22}Na photon in the gas results in electrons with a continuous spectrum of energies (Compton spectrum) and a peak corresponding to the photoelectric interactions. In addition, X-rays of energy around 30 keV are emitted as a consequence of the de-excitation of xenon after the interaction.

While the low energy photons and electrons can be considered as point-like particles, depositing all its energy in a small volume (which we often call a blob), higher energy electrons, in particular from the photo peak are extended objects, with a track length of the order of a few cm. It turns out, however, that most of the energy is deposited in a single blob, as the electron passes through the Bragg peak.

It is useful to assign spacial coordinates, as well as energy to the S_1 and S_2 signals before proceeding to a detailed reconstruction of the track topology. The simplest way to do this is to assign the z coordinate to the peak of the waveform (multiplied by the drift velocity) and then compute the x, y coordinates by a simple baricenter algorithm that uses the integral of the waveform.

$$\begin{aligned} x_b &= \frac{\sum_i x_i w_i A_i}{A} \\ y_b &= \frac{\sum_i y_i w_i A_i}{A} \end{aligned} \quad (3.2)$$

where w_i are the weights of the anode PMTs, A_i the total amplitude measured by each PMT (integral of the waveform), and $A = \sum_i w_i A_i$. The radial coordinate is then defined as:

$$R = \sqrt{(x_b^2 + y_b^2)} \quad (3.3)$$

We define two reference systems for the longitudinal coordinate. The so-called *light reference system*, z_l which starts at the energy plane (thus $z_l = 0$ corresponds to the position of the cathode PMTs), and the so-called *charge reference system*, z_c which starts at the EL grid (thus $z_c = 0$ corresponds to the position of the EL grid). Both reference systems are related by a trivial translation, $z_c = L - z_l$, where L is the light tube length (400 mm).

The reason to use two reference systems is as follows: when computing the attenuation of the S_1 signals as a function of the longitudinal coordinate, it is useful to use the light reference system (LRS), in which the LTF and LTTF are defined as $g_l(z_l = 0, r) = f_l(z_l = 0, r) = 1$. On the other hand, the ionization charge collected at the anode is maximum for zero drift (that is, near the anode itself). The charge reference system (CRS) is such that the function describing the attenuation of the charge with the drift length is $f_a(z_c = 0) = 1$.

The radial coordinate is defined at $R = \sqrt{(x_b^2 + y_b^2)}$, where x_b, y_b correspond to the baricenter.

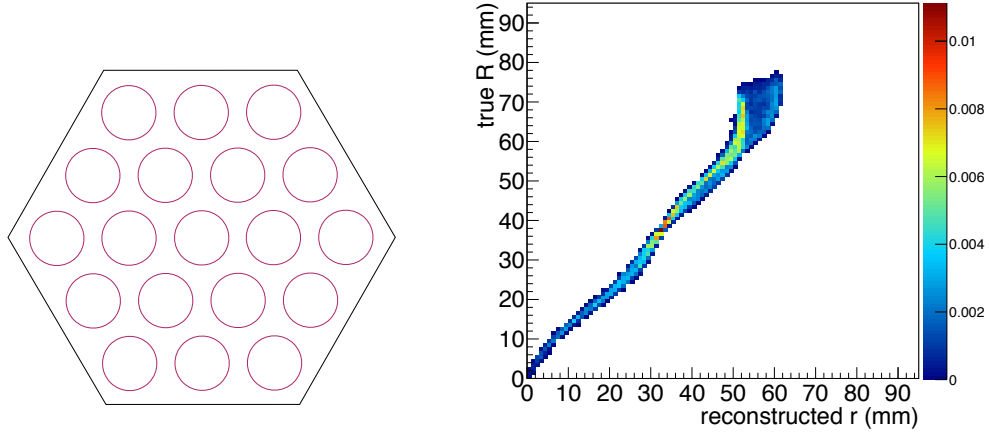


Figure 14. Left: a sketch of the tracking plane, showing the individual PMTs. Right: the relation between the reconstructed radius using the baricenter and the true radius for Monte Carlo simulated 511 keV electrons in the photo peak.

3.5 Definition of the fiducial volume

Figure 14 (right panel) shows the relation between the reconstructed radius using the baricenter and the true radius for Monte Carlo simulated 511 keV photoelectrons. Both radii are computed integrating the full S_2 signal of the electron —Thus, they represent, for all practical purposes the “average” transverse coordinate of the electron. Notice that the bias and dispersion of the baricenter are acceptably small for $R_{true} \sim R_{bar} \sim 20$ mm. This region corresponds to events that are defined primarily using the first and the second ring of PMTs. We call this “the core” of the fiducial volume. In the region up to $R_{bar} \sim 35$ mm, the baricenter shows some bias and the dispersion increases, but its behavior is still quite linear. This is the region where events are reconstructed using primarily the second and third ring of PMTs (left panel in figure 14). We call it “the shell” of the fiducial volume. For $R_{bar} > 35$ mm, the linearity and dispersion of the baricenter increases as the radius increases. This is not at all surprising, since this region corresponds to events which are primarily reconstructed using the third ring of PMTs. Since there is no fourth ring, as the events move away from the second ring to the third, the bias becomes larger and larger.

Therefore, the fiducial volume is defined as $R_{bar} < 35$ mm. Another way to describe our choice of the fiducial volume is to define it as the region in which the last ring of PMTs (which we call “the guard” ring) does not enter in the reconstruction of the transverse coordinate. Notice that the ratio of total volume to fiducial volume will improve as the detector becomes larger (since one is always giving up only the last ring, where the bias becomes very large due to the border effect described above). Notice also that a guard ring would be needed in a large detector using PMTs as a way of vetoing charged tracks emanating from the PV walls.

3.6 Primary scintillation

A physical process in the NEXT chamber, such as a genuine ^{136}Xe decay or the interaction of a photon, electron, or alpha particle due to a background or calibration event in the gas, results in the emission of prompt scintillation light (a pulse of about 20 nanoseconds) emitted in the VUV region, at a wavelength of around 172 nm.

329 The detection of the prompt scintillation light, S_1 , involves the following steps:

- 330 1. A physical interaction occurs in the chamber. For example, a 511 keV photon emitted by a
331 ^{22}Na source interacts in the xenon, depositing all its energy via a photoelectric interaction.
- 332 2. A number of primary scintillation photons are produced as a result of such interaction. The
333 average energy spent in the creation of one primary scintillation photon, W_s has been recently
334 measured [5] as

$$W_s = 76 \pm 6 \text{ eV} \quad (3.4)$$

335 this translates to $N_{\gamma_s} = 13\,158$ scintillation photons per MeV.

- 336 3. Photons are produced isotropically. In order to be detected they must reach the energy plane,
337 hit a PMT there and interact in the PMT photocathode.

338 All the above can be summarized as

$$n_{\gamma_s}^{pes}(z, R, r, \lambda) = N_{\gamma_s} \times \beta_l(z, R, r, \lambda) \quad (3.5)$$

339 where the function $\beta_l(z, R, r, \lambda)$ is a transfer function that takes into account the transport of the
340 photons from the production point to the energy plane, the fraction of the energy plane covered
341 by PMTs, the probability of a photon which hits a PMT to reach the PMT photocathode and the
342 quantum efficiency of the PMT. The transfer function depends on the longitudinal (z) and radial
343 (R) coordinates at which the photons are produced, the reflectivity (r) of the LT (or, in general, the
344 reflectivity of all the surfaces exposed to light in the chamber), the transparency of the electric grids
345 at the anode and cathode and the wavelength (λ) of the photons. It can be calculated by using our
346 full Monte Carlo simulation.

347 On the other hand, since we compute S_1 using all the PMTs in the energy plane, and taking into
348 account that the VUV light emitted in primary scintillation has a rather narrow peak at 172 nm, it
349 appears reasonable to integrate over R and λ . We can thus write:

$$N_{\gamma_s}^{pes}(z, r) = N_{\gamma_s} \times f_l(z, r) \quad (3.6)$$

350 where N_{γ_s} is the number of primary scintillation photons produced by a physical process and
351 $N_{\gamma_s}^{pes}(z, r)$ is the number of measured photoelectrons (by the PMTs of the energy plane). We call
352 $f_l(z, r)$ the *Light Transfer Function*, *LTF*. From Equation 3.6, we write:

$$f_l(z, r) = \frac{N_{\gamma_s}^{pes}(z, r)}{N_{\gamma_s}} \left(\frac{\text{pes}}{\text{photon}} \right) \quad (3.7)$$

353 Although the LTF can be numerically computed using our MC simulation, it admits an approxi-
354 mate deconvolution into three factors:

- 355 1. *The absorption of the photons in the light tube*: if the LT (or, in general, all the surfaces of the
356 chamber where a photon can be reflected) was lined with a perfect absorber, the z dependence
357 of the LTF would be simply described by solid angle (only the photons traveling directly to
358 the energy plane, without ever hitting the walls would be detected). Conversely, if the LT was
359 coated with a perfect reflector, the z dependence of the LTF would vanish (all the light would
360 be collected irrespectively of the position in which is produced).

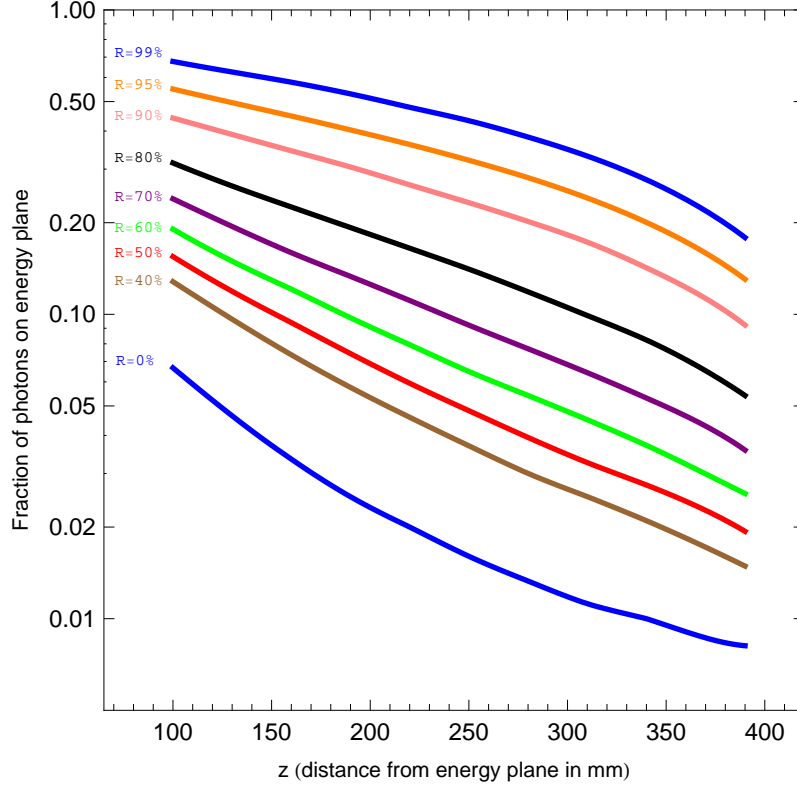


Figure 15. Light Tube Transfer Function (LTTF) $g_l(z, r)$ in NEXT-DEMO. Notice the log scale

2. The active area of the PMT plane, which is 40% in NEXT-DEMO.
3. The Quantum efficiency of the PMTs, which is 20% in the VUV region.

Then we can write:

$$N_{\gamma_s}^{pes}(z, r) = N_{\gamma_s} \times g_l(z, r) \times C \times Q_E \quad (3.8)$$

Notice that the product $N_{\gamma_s} \times C \times Q_E$ has units of photoelectrons. Therefore, the *Light Tube Transfer Function (LTTF)*, $g_l(z, r)$, defined as:

$$g_l(z, r) = \frac{N_{\gamma_s}^{pes}(z, r)}{N_{\gamma_s}} \frac{1}{C \times Q_E} \quad (3.9)$$

can be expressed as the fraction of the produced scintillating photons that create photoelectrons.

Figure 15 shows the LTTF as a function of the longitudinal coordinate z (in mm) for different values of the reflectivity r . Notice that the energy plane is located at $z = 0$ mm, while the cathode (and the beginning of the drift chamber and LT) is located at $z = 100$ mm. The anode (and the end of the LT) is located at $z = 400$ mm.

The use of a tagged source such as ^{22}Na enables the search for S_1 signals in a narrow time window defined by the NaI trigger. The signals are rather weak, only a few pes per PMT. Figure 16 shows the total charge of the S_1 signal (in photoelectrons) as a function of the longitudinal and radial coordinates for photoelectric events in the UVC. The left panel displays the S_1 total charge as

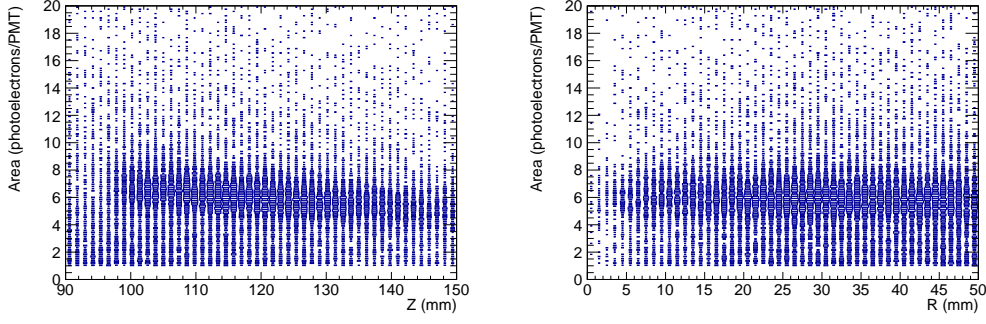


Figure 16. Position correlations for photoelectric events. Left: correlation between the S_1 total charge and the longitudinal position of the S_1 signals, z_l . Right: correlation between the total charge in the S_1 signal and the radial position.

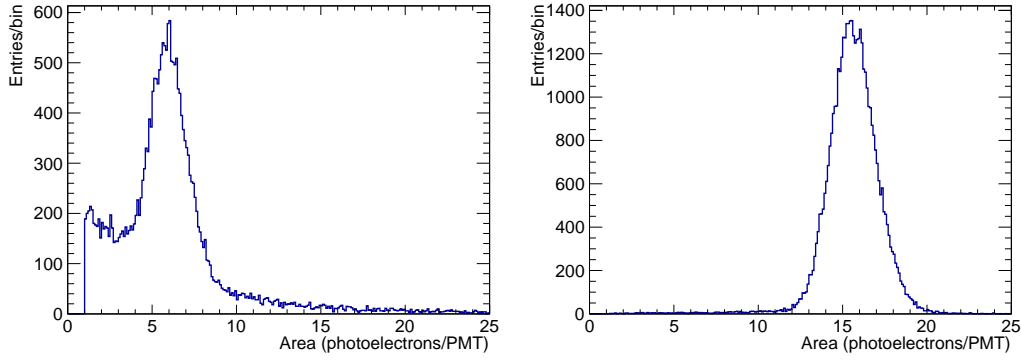


Figure 17. For photoelectric events, difference in the intensity of S_1 signals due to the TPB. Left: average value of the S_1 area for the VUC. Right: Same for BC.

a function of z_l , while the right panel displays the total charge as a function of R . The dependence of the S_1 charge with z can be expressed in terms of the LTF. As expected, the charge of S_1 depends very little of the radial coordinate. The average charge in the S_1 signal in the photo peak for the UVC is about of 6 pes/PMT.

The measurement of S_1 as a function of z_l permits the identification of the corresponding reflectivity curve in the LTF. Although this can be done by fitting the functional form of the LTF, we can take advantage of the fact that most of the interactions occur in a narrow longitudinal window corresponding to $z_l = 100$ mm (about 10 cm from the cathode plane) to use a simpler procedure. This procedure is described by the equation:

$$N_{\gamma_s}^{pes}(z_l = 100) = 6724 \times g(z_l = 100, r) \times 0.4 \times 0.2114 \text{ [pes]} \quad (3.10)$$

Since $N_{\gamma_s} = 0.511 \times 13158 = 6724$, $g(z_l = 100, r) = 114/537 = 0.21$. Read now the corresponding value in figure 15, to find that $g(z_l = 100, r = 0.6) \sim 0.2$. It follows that the reflectivity of the LT to the VUV light is $\sim 60\%$.

Figure 17 compares the total charge of the S_1 signal in the UV (LT not coated with TPB) and BC (light tube coated with TPB). The left panel shows the average value of the S_1 signal for photoelectric events in the UVC (~ 6 pes/PMT). The right panel shows it for the BC (~ 6 pes/PMT).

Coating with TPB results in improving the light collection at the cathode by a factor 3. Reading figure 15 now with $g(z_l = 100, r = 0.6) \sim 0.6$ yields a value of reflectivity of the LT in excess of 95%.

3.7 Secondary EL scintillation

In addition to the production of scintillation light, particle interactions in the chamber result in the ionization of the gas. The average energy spent in the creation of ionization pair, W_i is R&D [5] to be:

$$W_i = 22.4 \text{ eV} \quad (3.11)$$

Therefore, the number of ionization pairs per MeV is $N_e = 44462$. Those pairs drift under the action of the electric field applied to the detector. Electrons will drift towards the anode, at a velocity of about $1 \mu\text{s/mm}$ [Ref-Alpha-Paper], while positive ions will drift towards the cathode. Some of the electrons will be absorbed before reaching the anode, due to impurities in the gas. The number of electrons reaching the anode N_e^A is related with the number of primary electrons n_e , via:

$$N_e^A(z) = N_e \times f_a(z) \quad (3.12)$$

where $f_a(z)$ is a function that describes electron losses due primarily to electron attachment to gas impurities. $f_a(z)$ can be parameterized in terms of a quantity μ called the (drift) electron lifetime:

$$f_a(z) = e^{-\frac{z}{\lambda}} \quad (3.13)$$

Once the primary electrons reach the anode, they are accelerated between two parallel meshes, separated by a distance d . Denoting by E the electric field applied across those meshes, we can write the secondary scintillation yield Y [6] as:

$$\frac{Y}{p} = 140 \frac{E}{p} - 116 [\text{photons electron}^{-1} \text{ cm}^{-1} \text{ bar}^{-1}] \quad (3.14)$$

The quantity $\frac{Y}{p}$ called the reduced electroluminescence yield, is defined as the number of photons emitted per primary electron and per unit of drift length divided by the number density of the gas, N . The behavior of $\frac{Y}{p}$ with the reduced electric field, $\frac{E}{p}$ is linear above a threshold of about 0.5 kV/cm/bar.

In NEXT-DEMO the distance between the meshes is 0.5 cm, the typical operating pressure is 10 bar and the typical electric field across the grids was 12 kV. Those parameters correspond to $\frac{E}{p} = 2.4$, the same foreseen for NEXT-100. Applying then equation 3.14 we obtain a yield of 2480 photons per primary electron and centimeter, which corresponds to 1240 photons per primary electron across the EL region (0.5 cm). In terms of the yield (Y), and the distance between the grids (d), we can write the EL amplification function (ELAF) as:

$$y(E, p, d) = Y \times d [\text{EL photons}] \quad (3.15)$$

so that:

$$N_{\gamma_{EL}} = N_e \times f_a(z) \times y(E, p, d) \quad (3.16)$$

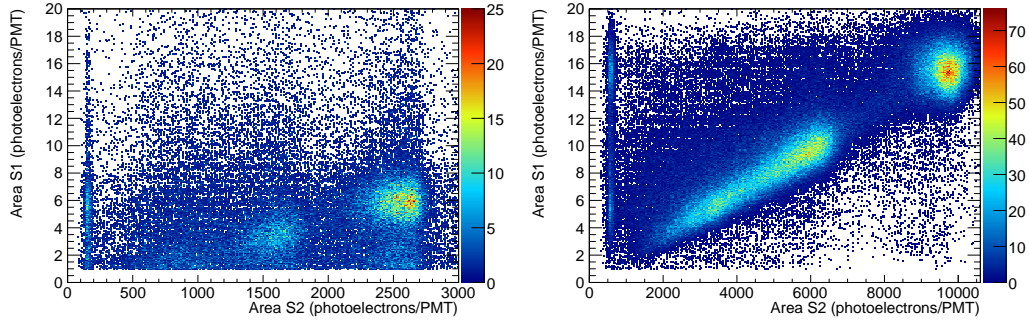


Figure 18. Correlation between the total charge of the S_1 and the S_2 signals. Left panel: for the UVC. Right panel: for the BC.

419 The number of photoelectrons produced per EL photon is related to the number of produced EL
420 photon via the LTF:

$$N_{\gamma_{EL}}^{pes}(z, r) = N_{\gamma_{EL}} \times f_l(z, r) \text{ [pes.]} \quad (3.17)$$

421 which is well approximated by:

$$N_{\gamma_{EL}}^{pes}(z, r) = N_{\gamma_{EL}} \times g_l(z, r) \times C \times Q_E \text{ [pes.]} \quad (3.18)$$

422 Let us compute the amount of light expected in the EL (S_2) signal, assuming a very long
423 electron lifetime, so that $f_a(z) = 1$.

$$N_{\gamma_{EL}}^{pes}(z_l = 400, r = 0.6) = N_{\gamma_{EL}} \times g_l(z_l = 400, r = 0.6) \times 0.4 \times 0.2 \text{ [pes]} \quad (3.19)$$

424 We can compute the number of secondary EL photons to be:

$$N_{\gamma_{EL}} = 22720 \times 1 \times 1240 = 2.8 \times 10^7 \text{ [EL photons]} \quad (3.20)$$

425 And read, from Figure 15, the function $g_l(z_l = 400, r = 0.6) = 0.025$. Putting everything
426 together we find $N_{\gamma_{EL}}^{pes} = 2.8 \times 10^7 \times 0.08 \times 0.03 = 56000$ pes or about 2950 pes/PMT.

427 Figure 18 shows the correlation between the total charge of the S_1 and the S_2 signals for
428 the UVC and the BC. The panel shows clearly the photoelectric peak, the Compton shoulder and
429 the x-ray escape peak. Notice that the value of the S_1 charge for the x-rays is the same as that
430 corresponding to the photoelectric peak. This is expected, as the x-ray is emitted by xenon de-
431 excitation in photoelectric events. Notice also that S_1 and S_2 show little correlation, as opposed to
432 the strong anti correlation measured in LXe TPCs [Reference to our alpha paper]. Last but not least,
433 the average value of S_2 signals for the BC is also a factor 3 higher than for the UVC.

434 4. Reconstruction of the energy spectrum

435 4.1 Fiducial containment condition

436 The left panel of figure 19 shows the raw spectrum recorded in the chamber, for the UVC. The
437 escape peak due to x rays emission is clearly visible, as well as the Compton spectrum. The

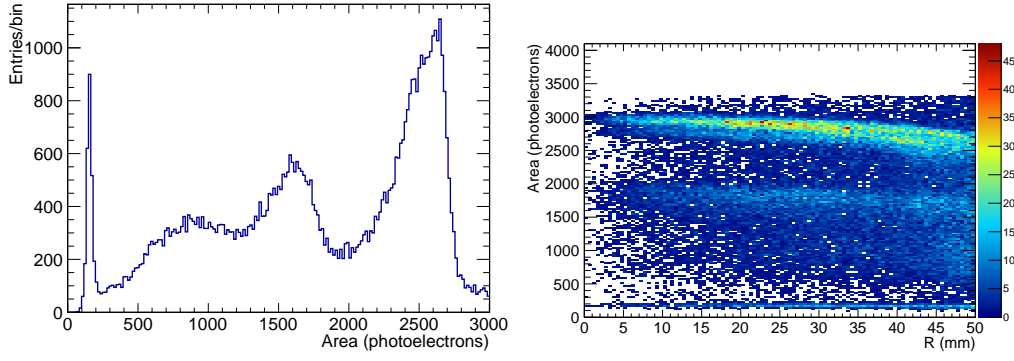


Figure 19. For the UVC. Left panel: Raw spectrum of selected events in the full chamber. Right panel: Energy of the events as a function of their radial position.

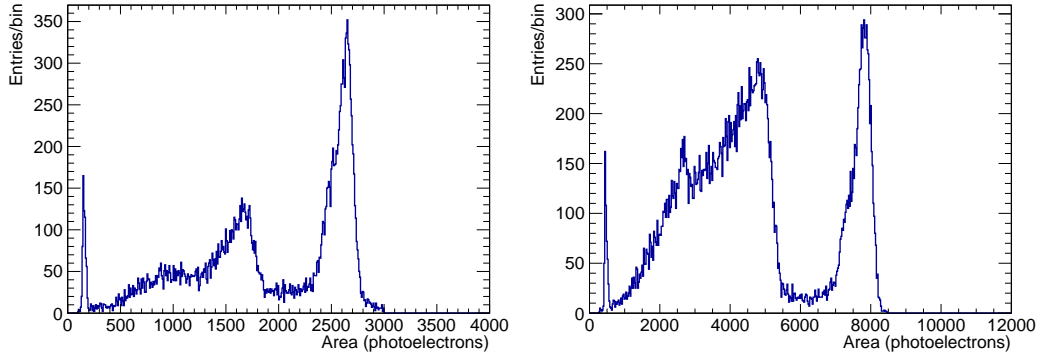


Figure 20. Energy of the events as a function of their radial position. Left panel: for the UVC. Right panel: for the BC.

photoelectric peak is very broad. The right panel of the figure shows the energy of the events as a function of their reconstructed radial position. The curve drops abruptly for large values of R , demonstrating that the interactions at large reconstructed radius are not fully contained.

The first step of the energy analysis is to “slice” the S_2 signal in portions $1 \mu\text{s}$ wide. For each one of these “slices”, a position $\mathbf{r} = (R, z)$ is found, in the same way that was used to determine the average position of the S_2 . We then impose the *fiducial containment condition*, FCC, which requires that all slices are contained in the fiducial region, defined as $\mathbf{r}_f = (R_f = 35, z_f^{\min} = 250, z_f^{\max} = 210)$, where the units are millimeters and we use the charge reference system to measure z . The FCC is:

$$\begin{aligned} z_f^{\min} &< z_i < z_f^{\max} \\ R_i &< R_f \end{aligned} \quad (4.1)$$

Figure 20 shows the raw spectrum after the FCC. The photoelectric peak becomes much sharper, but the resolution is still poor. In order to improve it, corrections are needed.

4.2 Geometrical corrections

Consider an electron produced by photoelectric interaction of a photon of 511 keV in the detector. Assume that we can determine the true (average) coordinates of the associated S_2 waveform, (x, y, z) .

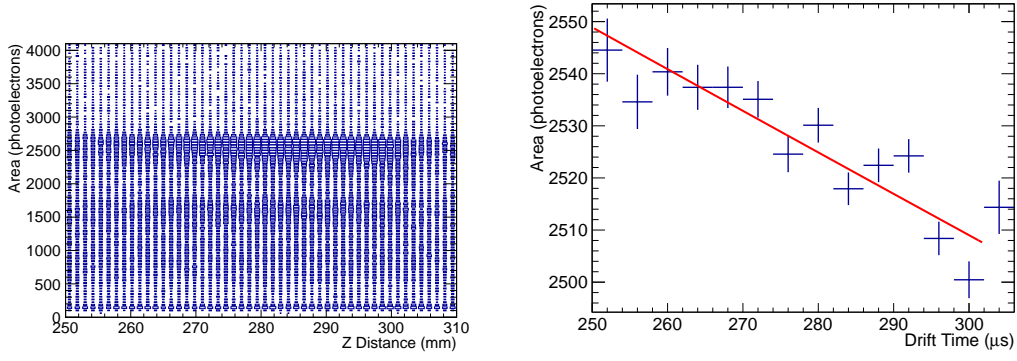


Figure 21. For the UVC. Left panel: correlation between the total charge of the S_2 signal and the longitudinal coordinate z_c . Right panel: exponential fit to the dependence of the total charge of photoelectric S_2 signals with the clock time t . The fit determines the inverse of the electron lifetime $1/\lambda$.

Assume also that the observed energy, E_{obs} , is measured after a refined calibration of the cathode PMTs, as described in previous sections. We define E_{rec} as an estimator of the true energy of the event obtained multiplying E_{obs} by a *detector response function* (*DRF*), η :

$$E_{rec} = E_{obs}(x, y, z) \times \eta(x, y, z) \quad (4.2)$$

The obvious problem with this definition is that the true position of the event is not known. Instead, we measure a reconstructed position (x_r, y_r, z_r) . As described in section 3 we compute z_r from the drift time and the drift velocity, and (x_r, y_r) using the baricenter. An exact calculation needs to take into account the bias of the position estimator. However, as shown in figure 14, the bias of the baricenter is small in the fiducial region, $R < 35$ mm.

It is assumed here that the electron track is small enough that the “blob” approximation holds and that the position of the electron can be described by the average position of the S_2 . This is only true if the electron track is small compared with the change of the DRF. Since the fiducial region is large compared with the transverse size of the electron tracks, the approximation is acceptable.

Finally, let us assume that the DRF can be factorized as:

$$\eta(x, y, z) = Z(z_r) \times \rho(R_r) \times \Phi(\phi_r) \quad (4.3)$$

where $Z(z_r)$ is a function that depends only on the reconstructed longitudinal coordinate, $\rho(R_r)$ is a function that depends only on the reconstructed radius ($R_r = \sqrt{x_r^2 + y_r^2}$) and $\Phi(\phi_r)$ is a function that depends only on the reconstructed azimuthal coordinate, $\phi_r = \tan^{-1} \frac{y_r}{x_r}$. We postulate that the geometrical corrections can be decomposed as the product of longitudinal, radial and an azimuthal corrections.

Obviously, this approximation only holds if the correlations between the corrections are small. This turns out, however, to be the case as will be demonstrated shortly.

4.3 Longitudinal corrections

Consider a photoelectric interaction of a 511 keV photon from the ^{22}Na source in the NEXT-DEMO chamber. Due to the electric field applied to the chamber, the ionization electrons will drift towards

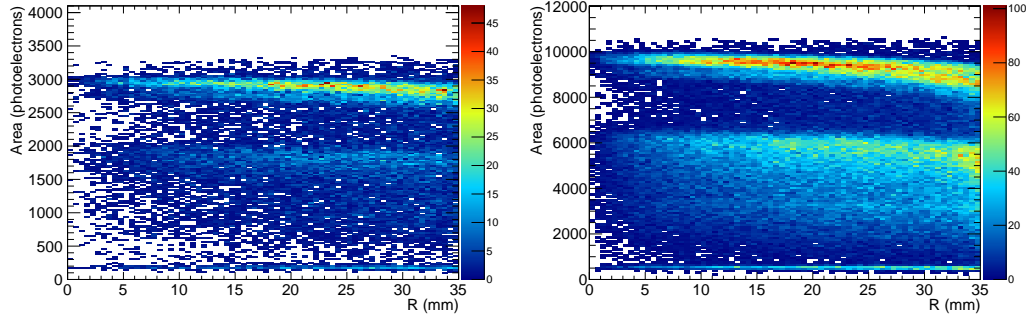


Figure 22. Distribution of the S_2 energy (in pes) as a function of R . Left panel: UVC. Right panel: BC.

the anode. The signal will be attenuated according to equation 3.13, introducing a dependence on z of the collected charge. Events happening very near the anode will deposit most of the charge in the collecting grids, while events happening near the cathode will loose some of it due of ionization electron attachment to the gas impurities.

The left panel of figure 21 shows the correlation between the longitudinal coordinate (e.g, z_c position) and the area of S_2 , in the area where the events are concentrated. As it can be seen the longitudinal dependence is rather soft, resulting in an almost flat function of the energy with z .

The longitudinal correction be determined from the data themselves by plotting the energy of the photoelectric S_2 signals as a function of the drift time and fitting an exponential law. This is shown in the right panel of figure 21. The fit yields the parameter $1/\lambda = 2 \times 10^{-4} \mu s$. The electron lifetime is, therefore, 4.0 ± 0.4 ms. This shows that the gas purity in the UVC period of NEXT-DEMO is very high. For the BC the electron lifetime was somewhat smaller. The most probable reason is the continuous degassing of water from the coated teflon panels. However, the lifetime was improving continuously during the run, confirming that very long lifetimes can be achieved by pumping continuously the gas through the hot getters over a sufficiently long period (weeks).

4.4 Radial and azimuthal corrections

Figure 22 shows the dependence of the energy with the radial position, for the UVC (left panel) and the BC(right panel) We can describe numerically the function $\rho(R_r)$ by fitting a spline through the data, as illustrated in figure 23 (top row, left panel) for the BC. The right panel of the same figure shows the data once corrected by $\rho(R_r)$.

The azimuthal correction is applied after the radial correction, in the same way, as illustrated in the bottom row of figure 23.

4.5 Energy resolution

Figure 24 shows the energy spectrum of ^{22}Na events in the whole fiducial region, $R < 35$ mm. The resolution of the photoelectric peak is 2.8% FWHM, for the UVC and 1.7% for the BC. This result is well reproduced by our Monte Carlo simulation of the detector, in which only geometrical effects are introduced (in the Monte Carlo run, the PMTs of the tracking and energy plane are all perfectly equalized and the lifetime of the electrons is arbitrarily long). The result also agrees with

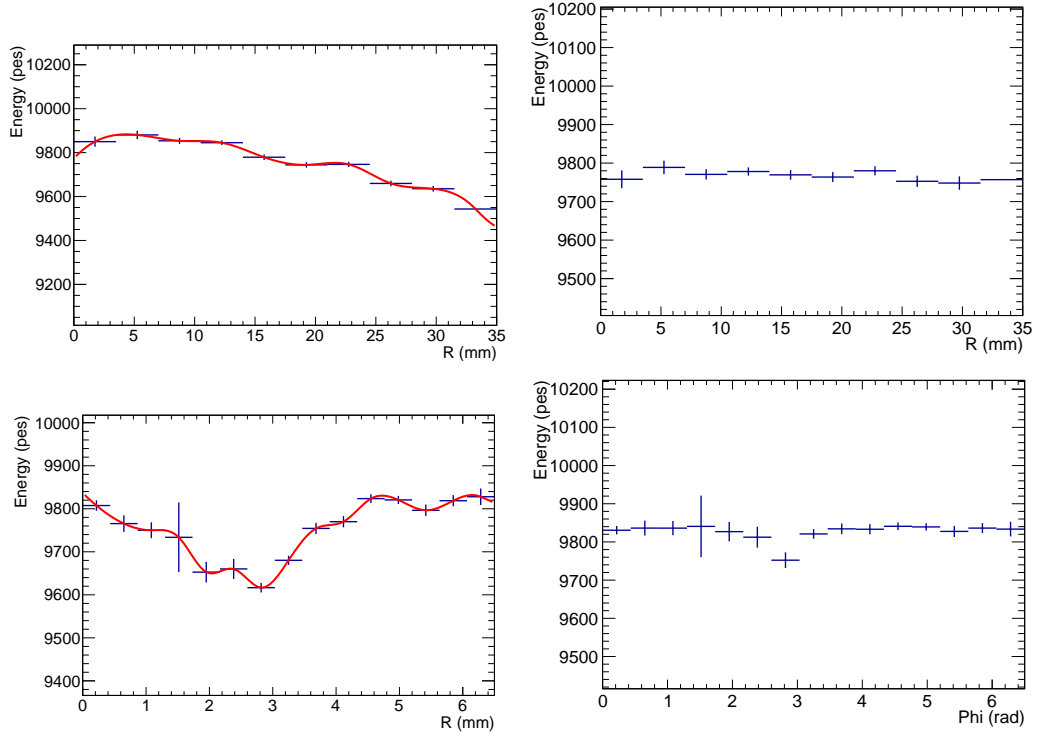


Figure 23. For the BC, top row: radial correction. Bottom row: azimuthal correction. Left panel: The correction is described by a spline fitted to the data. Right panel: The data after applying the correction.

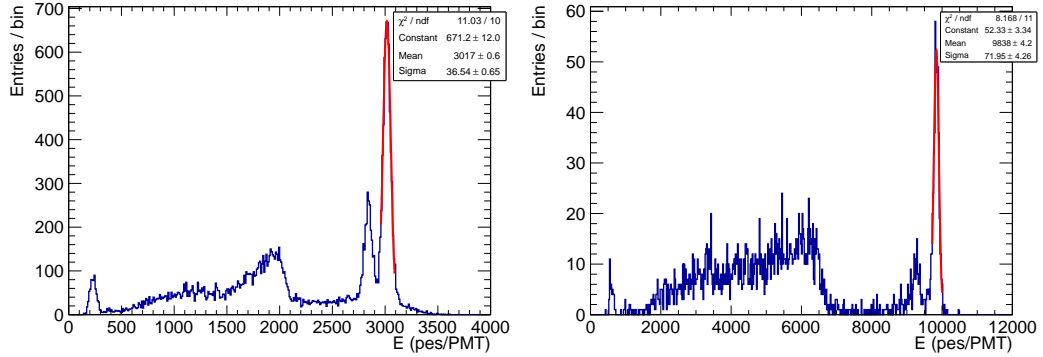


Figure 24. Energy spectrum of ^{22}Na events in the whole fiducial region ($R < 35$ mm). Left panel: UVC. Right panel: BC.

the expected scaling of photoelectron statistics, which is a factor three larger in the BC than in the UVC.

The photoelectron statistics of NEXT-100 will be very similar to that of NEXT-DEMO, about 10 pes per primary electron. The extrapolation to $Q_{\beta\beta}$ of the BC result, assuming a dependence proportional to $1/\sqrt{E}$ (a reasonable assumption, since the resolution of the photoelectric peak scales according to this law with the resolution of the X-ray escape peak) we obtain a resolution of 0.77%. This result improves the NEXT target of a resolution of 1% FWHM at $Q_{\beta\beta}$.

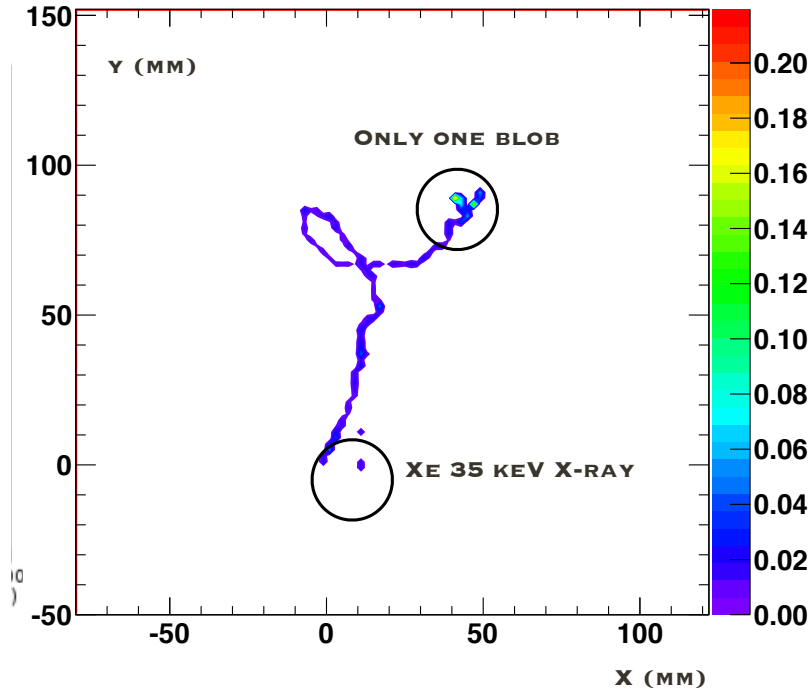


Figure 25. A Monte Carlo electron simulated in the NEXT-DEMO detector.

Thus, our first analysis with NEXT-DEMO shows clearly that NEXT target resolution can be achieved. On the other hand, there is much room for improvement. As discussed, the assumptions that we have made to correct the energy spectrum are approximations that can be refined, including a full treatment of the correlations and as well as taking into account the finite extension of the track. Work is in progress along these lines.

5. The topological signal

A major advantage of HPGXe chambers over LXe chambers is the availability to obtain a topological signature, which allows discriminating between the pattern associated to one electron (background events due mainly to photoelectric interactions of ^{214}Bi) and the pattern associated to two electrons (signal events arising from ^{136}Xe decays).

The trajectory of an electron propagating in the dense xenon gas of NEXT is a random walk due to the multiple scattering. In addition, each “point” of the “track” is seen by the light detectors as a “cloud” due to the longitudinal and transverse diffusion. Last, but not least, electrons radiate Bremsstrahlung photons. As a consequence, an electron in NEXT-DEMO looks as illustrated in Figure 25, a tortuous “tube of energy” ended in a “blob” corresponding to the Bragg peak. One can also often observe the x-ray emitted by xenon de-excitation.

The reconstruction of the track will be done of course with the tracking plane, but there is already important topological information that can be obtained from the energy plane. The S_2 signal is sampled in time slices (refer thereafter as “slices”) that correspond to the energy deposited by the

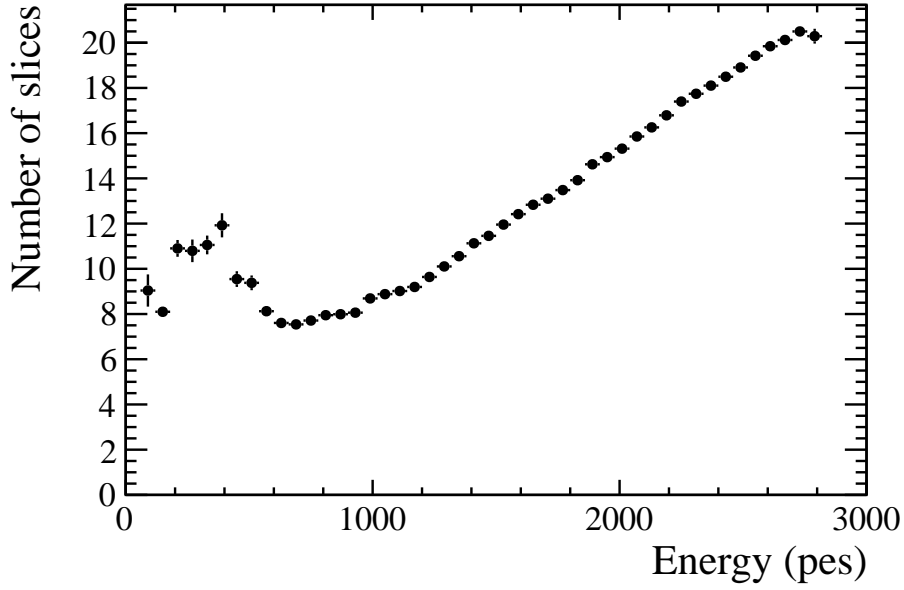


Figure 26. Average number of slices as a function of the energy.

529 track in a z section of the chamber. The sampling used in NEXT-DEMO is $1\ \mu\text{m}$ (or $1\ \text{mm}$ in z).
 530 This value is few times smaller than the resolution due by the diffusion of the electrons.

531 Figure 26 shows the average number of slices as a function of the energy. For energies below
 532 600 pes (100 keV) the number of slices is roughly constant with an average value of about 10. Since
 533 each slice has a width of $1\ \mu\text{s}$, we conclude that below some 100 keV, we are observing point-like
 534 objects whose width is of the order of $10\ \mu\text{s}$. This width comes about by the combination of two
 535 factors. The longitudinal diffusion, which is of the order of $3\ \mu\text{s}$ rms for blobs produced near the
 536 port where most of the signal is concentrated (thus the energy of point-like blob will be spread in
 537 about $9\ \mu\text{s}$, corresponding to a 3 rms integral of a the gaussian charge cloud) and the time needed to
 538 transverse the grid, which is also of the order of $3\text{--}4\ \mu\text{s}$. For energies above 600 pes the number of
 539 slices (and thus the length of the track) increases linearly although the slope is softer up to 1200 pes
 540 (or about 200 keV), than from 1200 pes onwards, an effect due to the fact that low energy electrons
 541 tend to deposit all its energy as a Bragg blob, while high energy electrons behave for a while like
 542 mips. The number of slices for electrons in the photo peak is of the order of 20, corresponding to
 543 electrons that travel about 2 cm in the longitudinal projection in the gas.

544 Figure 27 shows the average energy of the slices as a function of the time difference to the slice
 545 with maximum energy for S_2 signals within the photo-peak energy. One can identity two parts: a
 546 wide peak of 10 slices centered around the slice with the maximum energy and a “plateau” with
 547 several slices with low energies. We associate the two parts to the blob and the mip sections of
 548 the electron track respectively. The slice with the maximum energy has 400 pes and the slices in
 549 the “plateau” have less than 50 pes. Most of the energy of the S_2 signal (approximately 80%) is
 550 in the 10 slices of the blob. We have crudely estimated the number of blobs in the track using the
 551 following simple criteria to find a blob: there must be a slice with an energy at least 300 pes and
 552 whose neighbors slices have an energy greater than 50 pes. We have found that 98% of the times

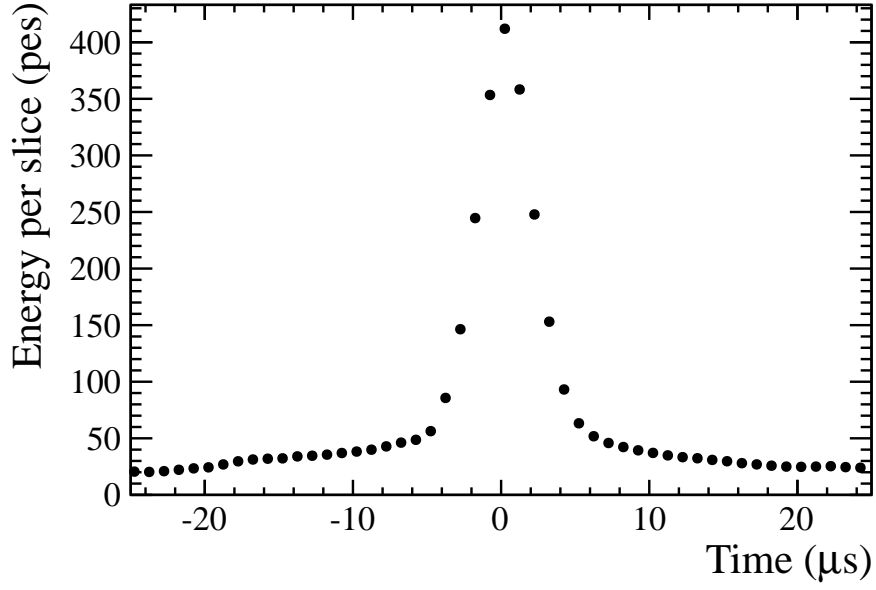


Figure 27. The energy of the slices as a function of the time difference to the slice with maximum energy.

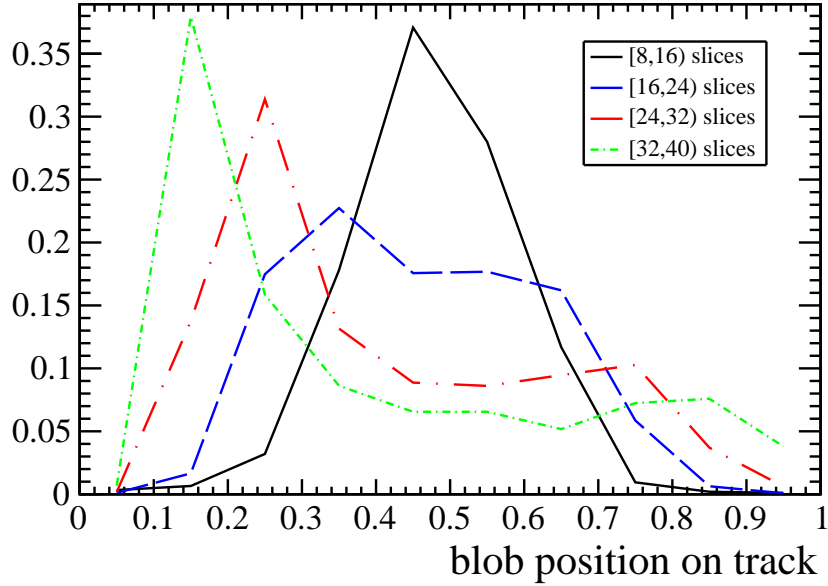


Figure 28. Relative position of the slice of maximum energy along the slices for different number of slices: [8,16) black; [16,24) red; [24,32) green; [32,40] blue.

553 there is only one blob and only 0.14 % two blobs. This is an impressive rejection factor of $O(10^{-3})$
 554 for almost no lost of efficiency.

555 We can study also where is the blob along the track using the information from the cathode. Fig
 556 28 shows the distribution of the relative position of the blob along the track (given as the position
 557 of the slice with the maximum energy with respect the number of slices) for tracks with different

numbers of slices. We expect that the blob will be center for short tracks (with low number of slices) and on the sides for long tracks (with large number of slices). Indeed, the blob is centered along the track when the number of slices is low, below 16. The track is just a blob. As the number of slices increases, tracks are more “horizontal”, and the blob move to the left. This is because in NEXT-DEMO electrons are produced close to the cathode, so only those electrons moving to the anode (to the left) are contained in the chamber while those moving to the cathode (to the right) are lost. In the case of tracks with large number of slices (>32) the blob is on the left most part to track, as expected.

In summary, the track topology can be characterized by looking at the time–coordinate. More information can be obtained by adding the transverse coordinates, which are, in particular, needed to impose that the electron is contained in the fiducial volume as well as to perform the radial corrections discussed in the previous section.

6. Summary and outlook

In this paper we have presented the initial results of the NEXT-DEMO detector, operated with a tracking plane made of PMTs and running in two configurations. Ultra violet (UVC), in which the light tube was uncoated, and blue (BC) in which the light tube was coated with TPB. The reflectivity of the LT has been found to be 60% in the UVC and more than 95% in the BC, demonstrating the rationale of TPB coating.

The detector response has been studies with a ^{22}Na source, for both the UVC and the BC. The S_1 and S_2 signals are found to be uncorrelated, as expected for electrons in high pressure gas. The measure electron lifetime is long, of the order of several milliseconds, showing the gas recirculation through hot getters, as foreseen for NEXT-100, effectively cleans up the gas impurities.

The spectrum of electrons produced by the interacting 512 keV gammas in the gas has been reconstructed, for both the UVC and the BC, in a large fiducial volume, as well as in a more central region. The resolution obtained in the BC, extrapolated to $Q_{\beta\beta}$, is 0.77% FWHM. This results improves considerably the target defined in our TDR of 1% FWHM at $Q_{\beta\beta}$, in spite of the simplicity of the corrections applied to the data. A more sophisticated treatment of the geometrical corrections is in progress, to further improve these results.

Initial studies concerning the reconstruction of the topology, in particular concerning the identification of the electron blob (the large energy deposit associated to the Bragg peak) have also been presented.

NEXT-DEMO is currently taking data with a plane made of SiPMs, and new results using this new tracking device are under preparation.

In summary, the first results of this large scale prototype show a robust and stable operation, with no leaks and a very low rate of sparks, improves the target energy resolution of NEXT in a large fiducial volume, and presents promising results that reinforce the strength of the topological signature.

Acknowledgments

This work was supported by the following agencies and institutions: the Spanish Ministerio de

597 Economía y Competitividad under grants CONSOLIDER-Ingenio 2010 CSD2008-0037 (CUP)
 598 and FPA2009-13697-C04-04; the Director, Office of Science, Office of Basic Energy Sciences, of
 599 the US Department of Energy under contract no. DE-AC02-05CH11231; and the Portuguese FCT
 600 and FEDER through the program COMPETE, project PTDC/FIS/103860/2008. J. Renner (LBNL)
 601 acknowledges the support of a US DOE NNSA Stewardship Science Graduate Fellowship under
 602 contract no. DE-FC52-08NA28752.

603 **References**

- 604 [1] **NEXT** Collaboration, V. Álvarez et al., *NEXT-100 Technical Design Report (TDR): Executive Summary*,
 605 *JINST* **7** (2012) T06001, [arXiv:1202.0721].
- 606 [2] J. J. Gómez-Cadenas, J. Martin-Albo, M. Mezzetto, F. Monrabal, and M. Sorel, *The search for*
 607 *neutrinoless double beta decay*, *Riv. Nuovo Cim.* **35** (2012) 29–98, [arXiv:1109.5515].
- 608 [3] D. Nygren, *High-pressure xenon gas electroluminescent TPC for Onu beta beta-decay search*, *Nucl.*
 609 *Instrum. Meth. A* **603** (2009) 337–348.
- 610 [4] **NEXT** Collaboration, V. Álvarez et al., *Near-Intrinsic Energy Resolution for 30 to 662 keV Gamma Rays*
 611 *in a High Pressure Xenon Electroluminescent TPC*, arXiv:1211.4474.
- 612 [5] L. Fernandes, E. Freitas, M. Ball, J. Gomez-Cadenas, C. Monteiro, et al., *Primary and secondary*
 613 *scintillation measurements in a xenon Gas Proportional Scintillation Counter*, *JINST* **5** (2010) P09006,
 614 [arXiv:1009.2719].
- 615 [6] C. Oliveira, M. Sorel, J. Martin-Albo, J. Gomez-Cadenas, A. Ferreira, et al., *Energy Resolution studies*
 616 *for NEXT*, *JINST* **6** (2011) P05007, [arXiv:1105.2954].